



NRC Publications Archive Archives des publications du CNRC

A study on fatigue crack growth behavior subjected to a single tensile overload : Part I : An overload-induced transient crack growth micromechanism

Lee, S. Y.; Liaw, P. K.; Choo, H.; Rogge, R. B.

This publication could be one of several versions: author's original, accepted manuscript or the publisher's version. / La version de cette publication peut être l'une des suivantes : la version prépublication de l'auteur, la version acceptée du manuscrit ou la version de l'éditeur.

For the publisher's version, please access the DOI link below. / Pour consulter la version de l'éditeur, utilisez le lien DOI ci-dessous.

Publisher's version / Version de l'éditeur:

<https://doi.org/10.1016/j.actamat.2010.09.049>

Acta Materialia, 59, 2, pp. 485-494, 2011-01-01

NRC Publications Record / Notice d'Archives des publications de CNRC:

<https://nrc-publications.canada.ca/eng/view/object/?id=042b0393-3081-494a-81e7-a68f3f1deca>

<https://publications-cnrc.canada.ca/fra/voir/objet/?id=042b0393-3081-494a-81e7-a68f3f1deca>

Access and use of this website and the material on it are subject to the Terms and Conditions set forth at

<https://nrc-publications.canada.ca/eng/copyright>

READ THESE TERMS AND CONDITIONS CAREFULLY BEFORE USING THIS WEBSITE.

L'accès à ce site Web et l'utilisation de son contenu sont assujettis aux conditions présentées dans le site

<https://publications-cnrc.canada.ca/fra/droits>

LISEZ CES CONDITIONS ATTENTIVEMENT AVANT D'UTILISER CE SITE WEB.

Questions? Contact the NRC Publications Archive team at

PublicationsArchive-ArchivesPublications@nrc-cnrc.gc.ca. If you wish to email the authors directly, please see the first page of the publication for their contact information.

Vous avez des questions? Nous pouvons vous aider. Pour communiquer directement avec un auteur, consultez la première page de la revue dans laquelle son article a été publié afin de trouver ses coordonnées. Si vous n'arrivez pas à les repérer, communiquez avec nous à PublicationsArchive-ArchivesPublications@nrc-cnrc.gc.ca.



A study on fatigue crack growth behavior subjected to a single tensile overload

Part I. An overload-induced transient crack growth micromechanism

S.Y. Lee^a, P.K. Liaw^{a,*}, H. Choo^a, R.B. Rogge^b

^a *Department of Materials Science and Engineering, The University of Tennessee, Knoxville, TN 37996, USA*

^b *Canadian Neutron Beam Centre, National Research Council Canada, Chalk River, ON, Canada K0J 1J0*

Received 19 January 2010; received in revised form 27 July 2010; accepted 22 September 2010

Available online 26 October 2010

Abstract

Neutron diffraction and electric potential experiments were carried out to investigate the growth behavior of a fatigue crack subjected to a single tensile overload. The specific objectives were to (i) probe the crack tip deformation and fracture behaviors under applied loads; (ii) examine the overload-induced transient crack growth micromechanism; (iii) validate the effective stress intensity factor range based on the crack closure approach as the fatigue crack tip driving force; and (iv) establish a quantitative relationship between the crack tip driving force and crack growth behavior. Immediately after a single tensile overload was introduced and then unloaded, the crack tip became blunt and enlarged compressive residual stresses in both magnitude and zone size were observed around the crack tip. The results show that the combined contributions of the overload-induced enlarged compressive residual stresses and crack tip blunting with secondary cracks are responsible for the observed changes in the crack opening load and the resultant post-overload transient crack growth behavior.

© 2010 Acta Materialia Inc. Published by Elsevier Ltd. All rights reserved.

Keywords: Fatigue crack growth; Overload; Crack closure; Electric potential; Neutron diffraction

1. Introduction

The effects of a single tensile overload on fatigue crack growth have been studied extensively since its discovery in the 1960s, due to the potential for the improvement of fatigue lifetime. The application of a single tensile overload during fatigue crack growth results in an instantaneous acceleration of the crack growth rate, followed by a large crack growth retardation period (i.e. the crack growth rate temporarily slows down), which increases the fatigue lifetime. There have been numerous efforts to account for the crack growth retardation phenomena, which include both experimental studies [1–16] and computer simulation studies [17–20]. Among them, the plasticity-induced crack

closure concept suggested by Elber [1] has been supported by many investigations [4–12,20]. Elber introduced the effective stress intensity factor range as a fatigue crack tip driving force, emphasizing the significance of a crack closure phenomenon in the wake of a crack. However, there exist many recent claims that deny the significance of crack closure. These suggest that a new approach is needed to describe the fatigue crack tip driving force [21–27]. Therefore, the exact retardation micromechanism, fatigue crack tip driving force and crack closure phenomenon still remain open questions. This might be due to experimental difficulties in measuring quantitative strain/stress fields near a fatigue crack tip under applied loads and observing in situ crack tip deformation and failure phenomena during real-time fatigue experiments.

A crack closure approach has played an important role in explaining many load–interaction effects on the fatigue

* Corresponding author.

E-mail address: pliaw@utk.edu (P.K. Liaw).

crack growth behavior under variable-amplitude loading [28]. The exact determination of crack opening and closing loads (or stresses) is important to predict accurate crack tip driving force. Most of the experimental crack closure measurements are based on the analysis of the specimen compliance, i.e. displacement/load [1,29–31]. An alternative method to measure crack closure is to employ the direct current potential drop (DCPD) technique. When a constant current is passed through the test specimen, the crack mouth potential is measured. The higher potential means the longer crack length due to an increased resistivity of the material. If a crack closes and yields an electric contact between the fracture surfaces, a crack closing (or opening) point should be determined from the curve of the applied load vs. potential during a single fatigue cycle. Recently, Andersson et al. [32] investigated the possibility of using DCPD for crack closure measurements by comparing closure results from in situ observations of crack closure using a scanning electron microscope. They found that the results of crack closure measurements made by the potential drop were similar to those determined from in situ scanning electron microscopy (SEM) observations, and concluded that a crack opening point is reliable if the crack closure is detected by potential measurements. In the current study, the crack tip deformation and fracture behaviors as well as the crack closure phenomena during a single loading–unloading cycle are investigated from the observation of changes in the electric potential using the DCPD method.

Recently, neutron diffraction and high-energy synchrotron X-ray diffraction as a nondestructive evaluation technique have been employed to investigate the overload effects during fatigue crack growth [14,15,26,33–36]. The deep-penetration and volume-averaging capabilities of these techniques enable the direct measurements of residual and internal strains/stresses in the bulk sample as a function of distance from the crack tip.

In summary, in situ monitoring of the crack tip deformation and failure characteristics during real-time fatigue experiments and simultaneous direct measurement of the evolution of stress/strain fields around a fatigue crack tip under applied loads are essential to a comprehensive understanding of the unresolved problems on fatigue crack propagation, such as the exact retardation micromechanism and the fatigue crack tip driving force, as well as the crack closure phenomenon. In this regard, neutron diffraction and electric potential investigations are reported here for: (i) probing in situ crack tip deformation and failure phenomena; (ii) examining the quantitative stress/strain fields near the crack tip under applied loads; (iii) elucidating the crack growth micromechanism of the cyclic deformation subjected to a single tensile overload; (iv) validating the effective stress intensity factor range based on the crack closure approach as the fatigue crack tip driving force; and (v) establishing a quantitative relationship between the crack tip driving force and crack propagation behavior. This first part of a two-part paper provides a fundamental understanding of the “overload-induced

transient crack growth micromechanism” by observing in situ crack opening/closing processes and residual stress distributions near the crack tip during fatigue crack propagation following a tensile overload. More specifically, this part presents the effects of residual stress and crack tip blunting on the crack opening load, the crack tip driving force and the crack growth behavior. In the companion paper (Part II [37]), in situ neutron diffraction is performed to observe the internal stress distributions near the crack tip under applied loads. Part II shows the “transfer phenomenon of stress concentration and its role in overload-induced transient crack growth”.

2. Experimental procedures

2.1. Fatigue crack growth experiments

The fatigue crack growth experiments were performed on a compact-tension (CT) specimen of HASTELLOY C-2000 alloy (56% Ni–23% Cr–16% Mo, in weight percent) using a computer-controlled Material Test System (MTS) servohydraulic machine. This material has a single-phase face-centered cubic structure, a yield strength of 393 MPa, an ultimate tensile strength of 731 MPa, a Young's modulus of 207 GPa and an average grain size of about 90 μm . The CT specimen geometry was prepared according to the American Society for Testing and Materials (ASTM) Standards E647-99 [38]. Before the crack growth tests, the CT specimens were precracked to approximately 1.27 mm. A constant load-range control (ΔP) mode was used for the crack growth tests with a frequency of 10 Hz and a load ratio, R , of 0.01 ($R = P_{\min}/P_{\max}$, P_{\min} and P_{\max} are the applied minimum and maximum loads of 72.5 N and 7250 N, respectively). The crack length was measured by a DCPD method [39,40], which is explained in more detail in Section 2.2. The stress intensity factor, K , was obtained using the following equation [38]:

$$K = \frac{P(2 + \alpha)}{B\sqrt{W}(1 - \alpha)^{3/2}} (0.886 + 4.64\alpha - 13.32\alpha^2 + 14.72\alpha^3 - 5.6\alpha^4) \quad (1)$$

where P = applied load, B = thickness, $\alpha = a/W$, a = crack length and W = width of a CT specimen.

When the crack length reached 20 mm during a constant-amplitude fatigue crack growth test, a single tensile overload (i.e. $P_{\text{overload}} = 10,875$ N, which is 150% of P_{\max}) was introduced and then the constant-amplitude fatigue crack growth test was resumed to monitor the subsequent crack growth behavior. Fig. 1 shows the crack growth rate (da/dN) vs. the stress intensity factor range, $\Delta K_{\text{applied}}$ ($=K_{\max} - K_{\min}$, K_{\max} and K_{\min} are the maximum and minimum stress intensity factors, respectively). The crack growth rate, da/dN , was obtained by a seven-point incremental polynomial technique [38]. After the application of a tensile overload, there was an initial acceleration of the crack growth rate followed by a large crack growth

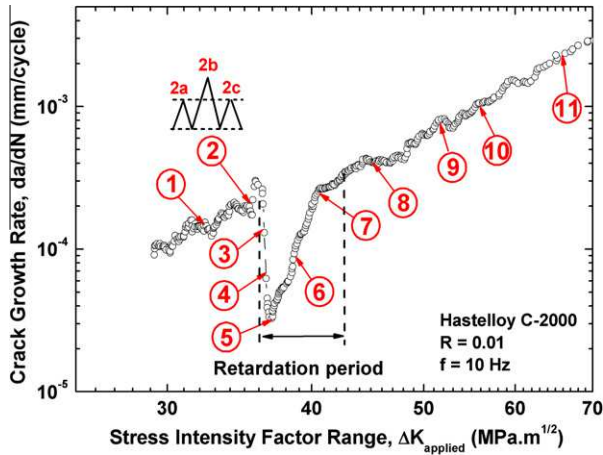


Fig. 1. The change in the crack growth rates, da/dN , as a function of the stress intensity factor range, $\Delta K_{\text{applied}}$.

retardation period. A total of 11 different crack growth stages were chosen to investigate such transient crack growth behaviors following a single tensile overload. The experimental details are summarized in Table 1.

The stage 1 ($\Delta K = 32.4 \text{ MPa m}^{1/2}$) was subjected to only cyclic deformation. When a fatigue crack reached $\Delta K = 35.9 \text{ MPa m}^{1/2}$, three fatigue cycles were continuously introduced: 2a – a fatigue cycle just before overloading; 2b – an overloading cycle; and 2c – a fatigue cycle right after overloading. After a single tensile overload was imposed, an initial acceleration of the crack growth rate was observed, and then the crack growth rate decreased sharply. Stages 3, 4 and 5 were prepared during a sharp reduction of the crack growth rate when a fatigue crack reached $\Delta K = 36.3$, 36.5 and $37.0 \text{ MPa m}^{1/2}$, respectively. After the minimum crack growth rate (stage 5) was observed, the crack growth rate gradually increased. Stages 6 and 7 were prepared during this increased period at $\Delta K = 38.6$ and $40.6 \text{ MPa m}^{1/2}$, respectively. Finally, the crack growth rate was recovered following the pre-overload slope in the da/dN vs. ΔK curve, and the crack growth rate increased linearly with increasing

ΔK . Stages 8–11 were prepared in this linear region at $\Delta K = 45.1$, 51.9 , 55.7 and $66.0 \text{ MPa m}^{1/2}$, respectively. The plastic zone sizes at each crack growth stage are estimated under plane strain ($\beta = 3$) and plane stress ($\beta = 1$) conditions following Irwin's approximation [41]; the range of plastic zone sizes is also indicated in Table 1.

Three different experimental approaches (see Table 1) were employed in this study: (i) electric potential (EP); (ii) neutron-diffraction residual stress mapping (ND-RS); and (iii) neutron diffraction in situ loading (ND-IL). This paper (Part I) will cover EP and ND-RS; Part II [37] will cover ND-IL. Note that respective measurements have been performed at the crack growth stages marked with a circle in Table 1. For example, only EP experiment was conducted at stage 1 and all three measurements (i.e. EP, ND-RS and ND-IL) were carried out at stage 5.

2.2. Electric potential experiments

In terms of an electric potential method, the measured dc electric potential at any crack length was normalized and converted into the corresponding crack length using Johnson's equation [39,40]:

$$a/W = 2/\pi \left[\frac{\pi}{2} - \arctan \left(\frac{Z}{\sqrt{1-Z^2}} \right) \right] \quad (2)$$

where

$$Z = \frac{e^{(\frac{h\pi}{W})} + e^{-(\frac{h\pi}{W})}}{e^{(U+X)} + e^{-(U+X)}} \quad (3)$$

and

$$X = \ln \left[\left(\frac{\left(e^{(\frac{h\pi}{W})} + e^{-(\frac{h\pi}{W})} \right)}{2 \cos \left(\frac{A_0}{W} \frac{\pi}{2} \right)} \right) + \sqrt{\left(\frac{\left(e^{(\frac{h\pi}{W})} + e^{-(\frac{h\pi}{W})} \right)}{2 \cos \left(\frac{A_0}{W} \frac{\pi}{2} \right)} \right)^2 - 1} \right] \quad (4)$$

Table 1

Details on 11 crack growth stages marked in Fig. 1 (F, fatigue; OL, overload; EP, electric potential; ND-RS, neutron-diffraction residual stress; ND-IL, neutron diffraction in situ loading).

Growth stages	Crack length (mm)	ΔK (MPa m ^{1/2})	Plastic zone size (mm)	Description	Various measurements		
					EP	ND-RS	ND-IL
1	18.00	32.4	0.74–2.21	F	O	–	–
2	20.00	35.9	0.90–2.71	2a (just before OL): F	O	O	O
			2.03–6.10	2b (during OL): F + OL	O	–	–
			0.90–2.71	2c (right after OL): F + OL + F	O	O	O
3	20.19	36.3	0.92–2.76	F + OL + F	O	–	–
4	20.33	36.5	0.93–2.80		O	–	–
5	20.60	37.0	0.96–2.88		O	O	O
6	21.40	38.6	1.05–3.14		O	O	O
7	22.30	40.6	1.15–3.46		O	O	O
8	24.20	45.1	1.43–4.28		O	–	–
9	26.50	51.9	1.88–5.65		O	–	O
10	27.60	55.7	2.17–6.52		O	–	–
11	30.00	66.0	3.05–9.16		O	–	–

Each experiment was carried out at the stage marked with “O”.

and a is the crack length, W is the specimen width, h is the distance between the two points at which the crack mouth potential is measured and U (=normalized potential) is defined as follows

$$U = \frac{PD_{\text{acttempcorrectedave}}/PD_{\text{initial}}}{PD_{\text{reftempcorrectedave}}/PD_{\text{refinitial}}} \quad (5)$$

PD_{initial} is the thermally corrected potential at some known initial crack length and $PD_{\text{refinitial}}$ is the thermally corrected initial potential of the reference probes.

When the reversing current is applied,

$$PD_{\text{acttempcorrectedave}} = (PD_{\text{ave+}} - PD_{\text{ave-}})/2 \quad (6)$$

$$PD_{\text{reftempcorrectedave}} = (PD_{\text{refave+}} - PD_{\text{refave-}})/2 \quad (7)$$

$PD_{\text{ave+}}$ and $PD_{\text{refave+}}$ are the sum of all PD readings from the crack mouth and reference probes, respectively, when the current is in one direction. $PD_{\text{ave-}}$ and $PD_{\text{refave-}}$ are the sum of all PD readings from the crack mouth and reference probes, respectively, when the current is in the other direction. This electric potential method as a bulk technique revealed the difference in crack length to be about 0.3 mm compared to that measured directly at the surface of the sample using SEM. From the observation of the fracture surface with the failed sample, it was found that the crack in the interior grew faster than that at the surface.

Using the electric potential method, an understanding of crack tip deformation and fracture behaviors during a single loading–unloading cycle can be enhanced from the observation of changes in the electric potential. More specifically, this technique enables the investigation of the crack closure phenomenon, as well as the elastic and plastic deformation behaviors at the crack tip under an applied load during a single cycle. In addition, respective crack opening loads at various crack growth stages can be determined from the curve of the normalized potential vs. applied load, as similarly shown in the previous work [42].

In this study, the changes in the electric potential during a single loading–unloading cycle were measured at 11 crack growth stages (see Fig. 1 and Table 1). From a plot of the normalized potential vs. the applied load, the bulk-averaged crack opening loads (COLs) were determined at various stages through the retardation period. Based on the measured COLs, the stress intensity factor at the crack tip opening, K_{op} , was calculated using Eq. (1). Thus, the effective stress intensity factor range, ΔK_{eff} , was obtained using the following equation:

$$\Delta K_{\text{eff}} = K_{\text{max}} - K_{\text{op}} \quad (8)$$

where K_{max} and K_{op} denote the stress intensity factors at the maximum load and crack opening, respectively. Finally, da/dN vs. ΔK_{eff} was plotted to investigate the applicability of ΔK_{eff} as a fatigue crack tip driving force.

2.3. Residual stress measurements using neutron diffraction

The spatially resolved neutron residual stress mapping was carried out on an L3 spectrometer at Chalk River

Laboratories, Canada. Three principal residual strain components (i.e. crack growth direction (ε_x), crack opening direction (ε_y) and through-thickness direction (ε_z) strains; Fig. 2a) were examined as a function of the position from the crack tip along the crack propagation direction (x -direction; Fig. 2b). Note that the crack tip identified at the surface of the sample using SEM was used for this measurement. A total of 26 points were measured as a function of distance from the crack tip. Scanning intervals of 1 mm from -4 to 0 mm (crack tip), 0.5 mm from 0 to 8 mm where sharp strain gradients are expected, 2 mm from 8 to 16 mm, and 3 mm from 16 to 22 mm were used to provide the required spatial resolution. The scattering volume was positioned in the middle of the sample thickness for all strain components (Fig. 2b). The ε_x strain component was measured using 1 mm wide and 2 mm tall (parallel to y) incident beam slits and a 1 mm wide diffracted beam slit. The ε_y and ε_z strain components were measured using 2 mm wide and 1 mm tall (parallel to x) incident beam slits and a 2 mm wide diffracted beam slit. The diffraction angles (2θ) for the ε_x , ε_y and ε_z strain components were 74° , 74° and 106° , respectively. Thus, the shape of the gauge volume for all three strain components was a parallelepiped elongated in the through-thickness direction (see Fig. 2b). Details of the neutron-diffraction residual stress measurements are presented elsewhere [43,44].

The d -spacings along the crack growth, crack opening and through-thickness directions were determined by the Gaussian fitting of the $\{3\ 1\ 1\}$ diffraction peak, and then the lattice strains were calculated as:

$$\varepsilon = (d - d_0)/d_0 \quad (9)$$

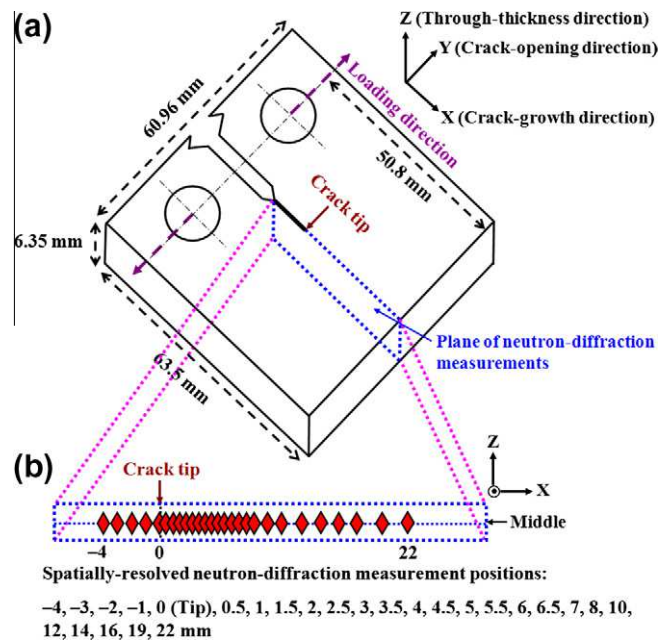


Fig. 2. Geometry of the specimen and lattice-strain measurement positions by neutron diffraction. (a) Schematic of a Hastelloy C-2000 compact-tension specimen; (b) spatially resolved neutron-diffraction measurement positions along the direction of the crack propagation (x).

where d_0 is the nominally stress-free reference lattice spacing measured 10 mm away from the corner of the specimen. Three residual stress components, σ_i ($i = x, y$ and z , corresponding to the crack growth, crack opening and through-thickness directions, respectively), were calculated from the three residual strain components using the following equation:

$$\sigma_i = \frac{E}{1+\nu} \left[\varepsilon_i + \frac{\nu}{1-2\nu} (\varepsilon_x + \varepsilon_y + \varepsilon_z) \right] \quad (10)$$

where E (=207 GPa) is the Young's modulus and ν (=0.3) is the Poisson's ratio. In this paper, the crack opening direction (σ_y) residual stress distributions near the crack tip are presented at various crack growth stages (i.e. 2a, 2c and 5–7; see Fig. 1 and Table 1).

3. Results

3.1. Overload-induced fatigue crack growth behavior

Fig. 1 shows the fatigue crack growth behavior following a single tensile overload as a function of the stress intensity factor range. Before the overload was applied at $\Delta K = 35.9 \text{ MPa m}^{1/2}$, the fatigue crack growth rate increased linearly with increasing ΔK . After the single tensile overload, four notable phenomena are observed: (i) an initial short acceleration of the crack growth rate immediately after the overload; (ii) a sharp decrease in the crack growth rate down to the minimum point; (iii) the gradual increase in the crack growth rate after passing the minimum point; and (iv) the recovery to the pre-overload slope in the crack growth rate.

3.2. Observation of the crack tip deformation and failure behaviors using electric potential

Fig. 3a shows the electric potential changes during a single loading–unloading cycle at the crack growth stage 2a (the cycle just before overloading; Fig. 1). Three distinct linear regions are observed from the plot of the normalized potential vs. the applied load. First, as the applied load increases up to $0.25P_{\max}$, the electric potential increased linearly. After a transition region is observed as the applied load increases from $0.25P_{\max}$ to $0.54P_{\max}$, a second linear region exhibiting a slight increase in the electric potential is observed as the applied load increases from $0.54P_{\max}$ to $0.83P_{\max}$. A third linear region is seen as a higher load is applied from $0.83P_{\max}$ to P_{\max} . During the unloading process, the electric potential is reduced following a reverse step.

Fig. 3b shows the potential change during a single tensile loading–unloading cycle at stage 2b (an overloading cycle; Fig. 1) and stage 5 (a maximum retardation point; Fig. 1). As the applied load increases up to $P_{\text{overload}} (=1.5P_{\max})$, the potential curve shows three distinct linear regions, similar to as described for stage 2a (Fig. 3a). However, a large normalized potential change of 0.04 is observed as the

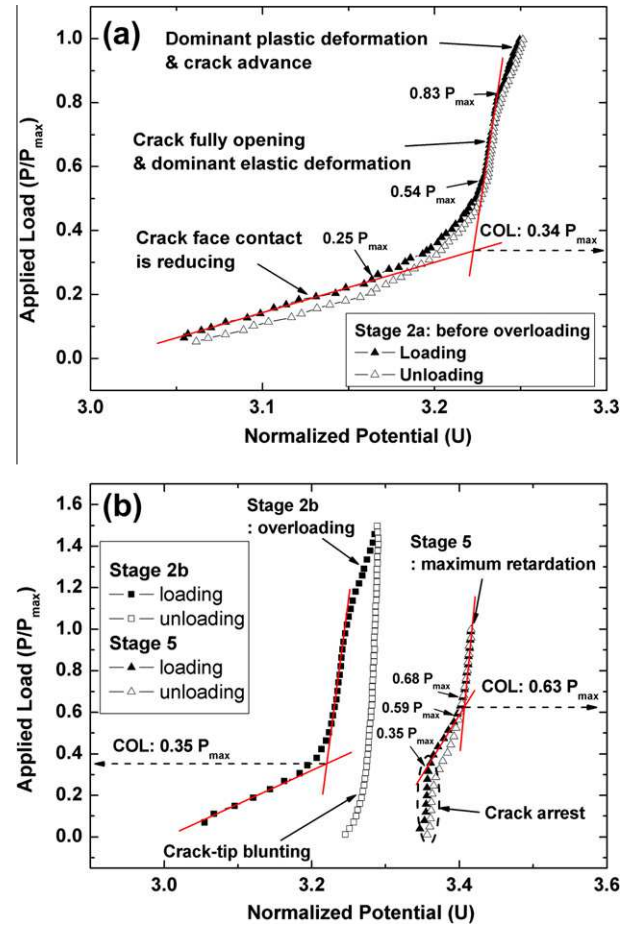


Fig. 3. Electric potential change during a single loading–unloading cycle (a) at stage 2a in Fig. 1, the cycle just before tensile overloading, and (b) at stages 2b (the cycle during overload) and 5 (a maximum retardation point) in Fig. 1.

applied load increases from P_{\max} to P_{overload} . During unloading, interestingly, the electric potential reveals an irreversible behavior. The potential slightly decreases, followed by a small transition region at a lower load.

The potential change at the maximum retardation (stage 5 marked in Fig. 1) is shown in Fig. 3b. This potential change shows quite a different behavior compared to that at stage 2a (Fig. 3a). When the load is increased up to $0.35P_{\max}$, the potential does not change. As a higher load is applied, the potential begins to increase linearly up to $0.59P_{\max}$, followed by a transition region ($0.59P_{\max}$ to $0.68P_{\max}$) and a slight increase in the potential ($0.68P_{\max}$ to P_{\max}). During unloading, the electric potential is reduced following a reverse step.

Fig. 4 shows SEM micrographs at the crack tip without load before and after the overload, and at stage 5. Before overloading (Fig. 4a), the crack is completely closed, whereas crack blunting is clearly observed with a few secondary cracks near the tip after overloading (Fig. 4b). Fig. 4c (stage 5) shows that the crack blunting remains and the fatigue crack is closed in the crack wake region, where further cyclic deformation is applied after the tensile overloading.

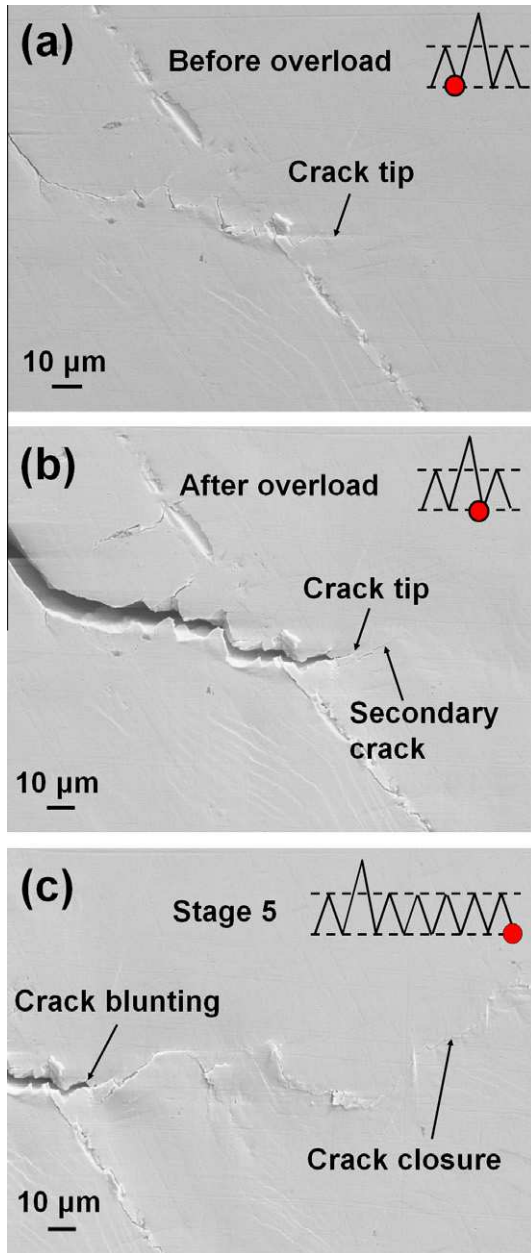


Fig. 4. SEM micrographs: (a) before overload, (b) after the overload and (c) at stage 5 in Fig. 1.

Fig. 5 shows the potential measurements during a single loading–unloading cycle at various crack growth stages marked in Fig. 1. Interestingly, at stages 5–7 (Fig. 1), the magnitude of the load at which the potential did not change during loading became smaller. Finally, the shape of a potential curve at stage 8 (Fig. 1) is similar to that at stage 1 and the first linear region in the potential curve gradually disappears as the crack propagates further (stages 9–11).

3.3. Residual stress measurements around a fatigue crack tip using neutron diffraction

Fig. 6 shows the crack opening direction (σ_y) residual stress distribution as a function of distance from the over-

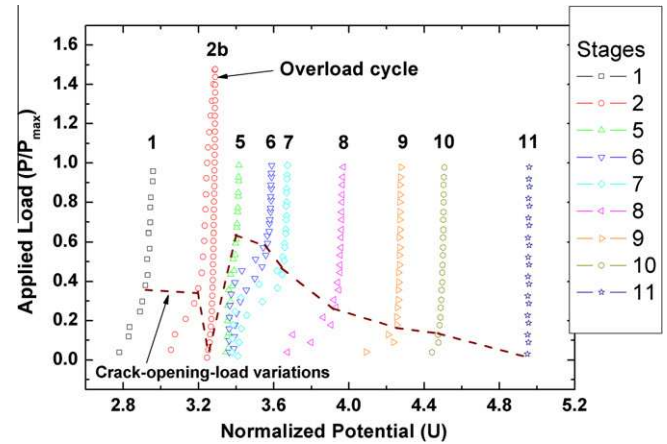


Fig. 5. Electric potential change during a single loading–unloading cycle at various crack growth stages marked in Fig. 1.

load point. Note that the overload point corresponds to the crack tip position at stage 2 (Fig. 1). In Fig. 6a, compressive residual stresses with a maximum of about -70 MPa are observed near a fatigue crack tip (-4 to 1 mm) at stage 2a, just before overload. After the single tensile overload is applied, much larger compressive residual stresses with a maximum of -225 MPa are observed within ± 4 mm from the crack tip. It is noted that our residual stress profile curves are in good qualitative agreement with those measured by Steuwer et al. [36]. As the sample cycles through the retardation period and the crack continues to advance, the compressive residual stresses relaxed and the positions of the compressive and tensile peaks shifted (Fig. 6b).

4. Discussion

4.1. Crack closure phenomena and crack opening load variations through the retardation period

The first linear region shown in Fig. 3a (P_{\min} to $0.25 P_{\max}$) during a loading cycle is related to a gradual crack opening from the crack closure in a fatigue wake, i.e. the disappearance of the crack face contact. In other words, the closed crack face (shown in Fig. 4a) from the previous unloading cycle begins to open with increasing applied load, resulting in a significant change in the electric potential. The second linear region ($0.54 P_{\max}$ to $0.83 P_{\max}$) might be due to the dominant elastic deformation, after the crack tip is fully open. The transition region between the two linear regions may be attributed to different crack opening levels between the surface and interior of the material, since the electric potential measurement shows the bulk response of the material. The third linear region ($0.83 P_{\max}$ to P_{\max}) results from the actual crack length increment accompanying the dominant plastic deformation at the crack tip. From such potential measurements during a loading cycle, the bulk-averaged COL can be determined by a fitting of the first and second linear regions. Thus, a COL of $0.34 P_{\max}$ was determined for stage 2a (Fig. 1). During

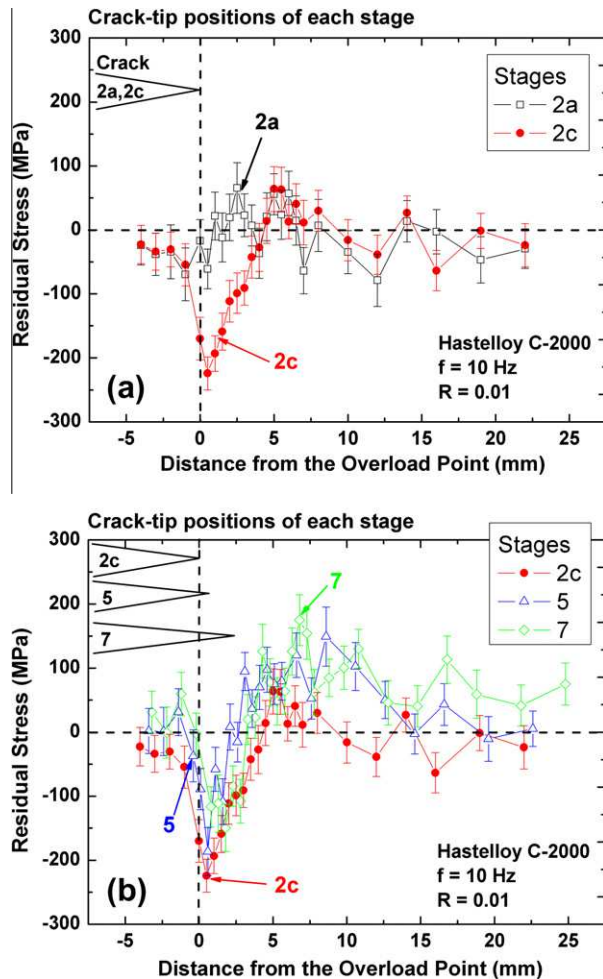


Fig. 6. Crack-opening direction (σ_y) residual stress distributions as a function of distance from the overload point at various crack growth stages in Fig. 1. (a) σ_y residual stress profiles at stages 2a and 2c in Fig. 1; (b) σ_y residual stress profiles at stages 2c, 5, and 7 in Fig. 1.

unloading, the crack face is closed again, following a reverse step.

The large normalized potential change of 0.04 seen at stage 2b (during overloading; Fig. 3b) reveals that a tensile overload resulted in a larger advance of the crack with more plastic deformation than that observed in the immediately preceding cycle. During unloading, the potential was slightly reduced due to elastic unloading, followed by a small transition region at a lower load. As a result, there is no crack closure in a crack wake region and the only new crack face created by an overload was closed, showing a small transition region. In order to confirm the results of the potential measurement, the shape of a crack tip was investigated using SEM. Immediately after overloading, crack blunting with small secondary cracks was observed, confirming that there was no crack closure behind the crack tip.

At stage 5 (a maximum retardation point; Fig. 1), a “crack arrest” phenomenon was clearly observed below $0.35P_{\max}$. It means that the closed crack face (Fig. 4c) between the crack blunting region and actual crack tip

position did not open, as the load increases up to $0.35P_{\max}$. As a higher load was introduced, the electric potential began to increase linearly ($0.35P_{\max}$ to $0.59P_{\max}$), followed by a transition region ($0.59P_{\max}$ to $0.68P_{\max}$) and a slight increase in the potential ($0.68P_{\max}$ to P_{\max}), corresponding to the gradual closed-crack opening, the crack tip fully opening and the dominant elastic deformation, respectively. Hence, a high COL of $0.63P_{\max}$ was obtained at the maximum retardation point (stage 5; Fig. 1). During unloading, the crack closed again, following a reverse step of a loading curve.

Potential measurements at various crack growth stages marked in Fig. 1 were put together for comparison, as shown in Fig. 5. At stage 1 (constant-amplitude fatigue crack growth before overloading), a loading–unloading potential curve showed the reversible behavior and a COL of $0.34P_{\max}$ was measured. At stage 2b (the overloading cycle; Fig. 1), the potential curve showed the irreversible behavior, indicating that the crack closure did not occur and the COL decreased sharply down. As the crack propagated to stage 5 (maximum retardation point; Fig. 1), the largest crack arrest portion appeared up to $0.35P_{\max}$, and the highest COL of $0.63P_{\max}$ was found. When the crack grew from stage 5 to stage 8, the crack arrest portion became smaller, disappearing completely at stage 8. This corresponds to a gradual decrease in the COL. Finally, the shape of the potential curve at stage 8 was similar to that at stage 1. This is consistent with the crack growth rate fully recovering to the pre-overload slope (see Fig. 1). As the crack grew further to stage 11, the COL was gradually reduced, eventually to zero. It should be noted that such changes in the COL are related to the experimentally measured crack growth rate (Fig. 1).

4.2. Correlation between the crack growth behavior and ΔK_{eff}

Four distinct slopes from the curve of da/dN vs. $\Delta K_{\text{applied}}$ were found, as shown in Fig. 1: (Case 1) a slope (between stages 1 and 2a, and between stages 8 and 11) from pre-overload constant-amplitude crack growth; (Case 2) a slope indicating an initial acceleration immediately after the tensile overloading; (Case 3) a slope showing a sharp decrease between stages 3 and 5; (Case 4) a slope between stages 5 and 7, which is larger than that in the Case 1 but smaller than that in Case 3. Note that the slope changes in crack growth rate (Fig. 1) are closely associated with those of the ΔK_{eff} (Fig. 7a), which is a function of the COL. As shown in Fig. 5, the COLs in the constant-amplitude crack growth slowly decreased with increasing ΔK (see the COL change in stages 1–2a and 8–11), and thus the ΔK_{eff} also increased slowly. After the single tensile overload, a very low COL was obtained, resulting in a sharp increase in ΔK_{eff} (Fig. 7a). In Case 3, the COL sharply increased with a short increment of crack length (i.e. 0.6 mm from an overload point), which resulted in a sharp decrease in ΔK_{eff} . Likewise, in Case 4, the gradual decrease in COL, which has higher reduction rate than that of Case

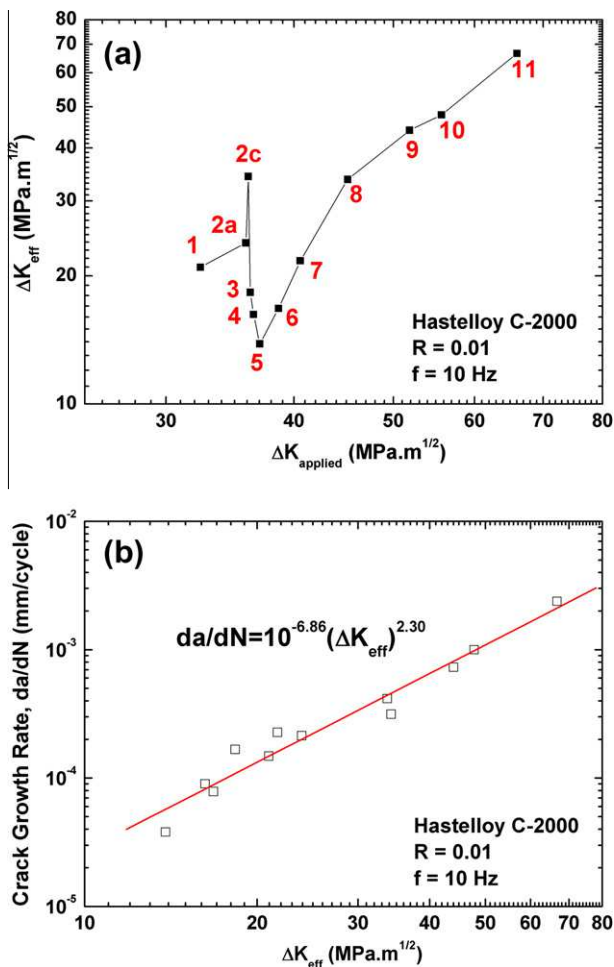


Fig. 7. Correlation between effective stress intensity factor range and measured crack growth rates. (a) Effective stress intensity factor range, ΔK_{eff} , vs. applied stress intensity factor range, $\Delta K_{\text{applied}}$; (b) crack growth rate, da/dN , vs. effective stress intensity factor range, ΔK_{eff} , at various crack growth stages marked in Fig. 1.

1, was examined. Thus, an increase rate in the ΔK_{eff} from stage 5 to stage 7 is larger than that of Case 1.

To investigate the applicability of ΔK_{eff} as the actual fatigue crack tip driving force, the crack growth rate (da/dN) was plotted as a function of the ΔK_{eff} , as presented in Fig. 7b. The crack growth rate had a good linear correlation with the ΔK_{eff} , which suggests that the ΔK_{eff} can be considered as the fatigue crack tip driving force.

4.3. Effects of compressive residual stress and crack tip blunting on the crack opening load

After a single tensile overload was applied, the COLs changed gradually from stage 2c to stage 8, as exhibited in Fig. 5. The changes of COL within this period are associated with the combined contributions of enlarged compressive residual stresses and crack tip blunting with secondary cracks (i.e. changes in the crack tip geometry). Immediately after the tensile overload, enlarged compressive residual-stress fields were observed near the crack tip (Fig. 6a). Although these compressive residual-stress fields

relax with crack propagation through the overload-induced plastic zone (Fig. 6b), the fatigue crack should overcome these stress fields applied in the wake of the crack to make the crack tip fully open. Thus, a higher COL would be required under the enlarged compressive residual-stress fields. Furthermore, the observed crack arrest load of $0.35P_{\text{max}}$ at stage 5 (Fig. 3b) would be associated with a load value to remove the enlarged compressive residual-stress field.

Crack tip blunting could be considered as another factor influencing the crack arrest and the change in the COL. It is known that crack tip blunting behaves like a notch. As a load is applied, the stress field would be initially concentrated near a blunting region (an overload point), reducing the actual magnitude of the stresses applied in a crack wake as well as at the crack tip. The crack branching (or secondary cracks) [6,7] that occasionally occurs immediately after the overload could partially contribute to the reduction of the stresses in a wake region by maximizing the blunting effect. Hence, a higher applied load would be required to reach stress fields large enough to open the closed crack face. If large compressive residual stresses are also introduced in the closed crack ahead of the blunting region, a much higher load should be imposed to reach a certain critical stress value to open the closed crack face. Therefore, the crack arrest phenomena could be observed until such a required stress value is obtained. It is suggested that the crack arrest phenomena observed in the retardation period result from the combined contributions of the enlarged compressive residual stresses and crack tip blunting with secondary cracks.

It should be noted that these combined effects on the COL depend on the crack length grown from the blunt crack (an overload point). If the crack grows very little from the blunt crack (i.e. the initial acceleration period shown in Fig. 1), the crack face will be open with a lower applied load due to high stress concentration in the blunting region and, thus, the crack tip will experience much higher stress compared to that just before overloading. The increased stresses would lead to an initial short period of accelerated crack growth rate. Moreover, secondary cracks in front of the blunt crack that often occur after overloading (Fig. 4b) could help accelerate the crack growth rate by coalescence with the primary crack, as exhibited in Fig. 4c. As the crack length increases from stage 3 to stage 5 (Fig. 1), the influence of the combined effects on the crack arrest load and COL becomes more significant, as revealed by the highest crack arrest load and COL at stage 5 (Fig. 5). The maximum retardation (stage 5; Fig. 1) is usually observed at 0.3–0.6 mm from the overload point. This might be thought of as a critical point where the combined contributions of enlarged compressive residual stresses and crack tip blunting are maximized. In contrast, as the crack grows far away from an overload point (i.e. from stage 5 to stage 7; Fig. 1), the combined effects on the COL become smaller and thus the stresses can concentrate at the crack tip with a lower load. When

these combined effects completely disappear (stage 8; Fig. 5), the crack growth rates are fully recovered following a pre-overload slope (stage 8; Fig. 1).

It would be interesting to investigate the relationship between the overload-induced plastic zone and subsequent fatigue-induced plastic zone at a recovery point of the crack growth rate. The overload-induced plastic zone size of about 5 mm was estimated from the crack opening direction (σ_y) residual stress profile ahead of the crack tip (stage 2c in Fig. 6a), as previously studied by Rice [45]. The parameter $\beta = 1.22$, related to the stress state, was determined using estimated plastic zone size (i.e. 5 mm) and Irwin's approximation [41]. Assuming that β does not change much as the crack propagates through the overload plastic zone, a fatigue-induced plastic zone size of 3.2 mm was obtained at a crack length of 23.4 mm (i.e. the crack length at the recovery point of the crack growth rate; Fig. 1). It was found that, when the crack growth rate was fully recovered, the fatigue crack was still within the overload-induced plastic zone and a part of the fatigue-induced current plastic zone grew out of the overload-induced zone.

In summary, the combined effects of overload-induced enlarged compressive residual stresses and crack tip blunting with secondary cracks (i.e. changes in the crack tip geometry) are responsible for the observed changes in the COL and resultant post-overload transient crack growth behavior, based on the crack closure approach. When these combined effects completely disappear or are sufficiently small, the crack growth rate returns to the pre-overload behavior.

5. Conclusions

Electric potential and neutron diffraction experiments were carried out to investigate overload-induced transient crack growth behavior. The main results are summarized as follows:

1. In the unloaded condition immediately following the tensile overload, the crack tip became blunt and enlarged compressive residual stresses with a maximum of -225 MPa were observed within ± 4 mm from the crack tip.
2. An initial acceleration of the crack growth rate might be due to the high stress concentration in the crack blunting region and coalescence of secondary cracks with the primary crack.
3. In the maximum retardation point (stage 5; Fig. 1), the highest crack arrest load and crack opening load were examined, indicating the smallest ΔK_{eff} value.
4. As the crack propagates into the overload-induced plastic zone, the compressive residual stresses are relaxed and the positions of the compressive and tensile peaks shift.
5. The post-overload transient crack growth rates were normalized with the ΔK_{eff} , which suggests that it can be considered as the fatigue crack tip driving force.
6. The results show that the combined effects of overload-induced enlarged compressive residual stresses and crack tip blunting with secondary cracks are responsible for the observed changes in the crack opening load and resultant post-overload transient crack growth behavior, based on the crack closure approach.

Acknowledgements

This work was supported by the US National Science Foundation (NSF), under DMR-0231320, CMMI-0900271 and DMR-0909037, with Drs. C. Huber, D. Finotello, C.V. Cooper and A. Ardell as contract monitors. The authors would also like to thank Dr. Klarstrom of Haynes International, Inc. for providing the test materials, and Mr. D. Fielden and Dr. M. Gharghoury for their help during experiments.

References

- [1] Elber W. ASTM STP 486; 1971. p. 230–42.
- [2] Wheeler OE. J Basic Eng 1972;94:181–6.
- [3] Jones RE. Eng Fract Mech 1973;5:585–604.
- [4] Gan D, Weertman J. Eng Fract Mech 1981;15:87–106.
- [5] Newman Jr JC. ASTM STP 748; 1981. p. 53–84.
- [6] Suresh S. Scripta Metall 1982;16:995–9.
- [7] Suresh S. Eng Fract Mech 1983;18:577–93.
- [8] Ward-Close CM, Blom AF, Ritchie RO. Eng Fract Mech 1989;32:613–38.
- [9] Shin CS, Hsu SH. Int J Fatigue 1993;15:181–92.
- [10] Dougherty JD, Srivatsan TS, Padovan J. Eng Fract Mech 1997;56:167–87.
- [11] Borrego LP, Ferreira JM, Pinho da Cruz JM, Costa JM. Eng Fract Mech 2003;70:1379–97.
- [12] Makabe C, Purnowidodo A, McEvily AJ. Int J Fatigue 2004;26:1341–8.
- [13] Bichler Ch, Phippan R. Eng Fract Mech 2007;74:1344–59.
- [14] Lee SY, Barabash RI, Chung JS, Liaw PK, Choo H, Sun Y, et al. Metall Mater Trans A 2008;39:3164–9.
- [15] Lee SY, Choo H, Liaw PK, Oliver EC, Paradowska AM. Scripta Mater 2009;60:866–9.
- [16] Codrington J, Kotousov A. Eng Fract Mech 2009;76:1667–82.
- [17] Zhang X, Chan ASL, Davies GAO. Eng Fract Mech 1992;42:305–21.
- [18] Pommier S, De Freitas M. Fatigue Fract Eng Mater Struct 2002;25:709–22.
- [19] Roychowdhury S, Dodds Jr RH. Fatigue Fract Eng Mater Struct 2005;28:891–907.
- [20] Singh KD, Khori KH, Sinclair I. Acta Mater 2006;54:4393–403.
- [21] Vasudevan AK, Sadananda K, Louat N. Scripta Metall Mater 1992;27:1673–8.
- [22] Louat N, Sadananda K, Duesbery M, Vasudevan AK. Metall Trans A 1993;24:2225–32.
- [23] Vasudevan AK, Sadananda K, Louat N. Mater Sci Eng A 1994;188:1–22.
- [24] Sadananda K, Vasudevan AK, Holz RL, Lee EU. Int J Fatigue 1999;21:233–46.
- [25] Zhang J, He XD, Du SY. Int J Fatigue 2005;27:1314–8.
- [26] Croft MC, Jisrawi NM, Zhong Z, Holtz RL, Sadananda K, Skaritka JR, et al. Int J Fatigue 2007;29:1726–36.
- [27] Vallellano C, Vazquez J, Navarro A, Dominguez J. Fatigue Fract Eng Mater Struct 2009;32:515–24.
- [28] Schijve J. ASTM STP 982; 1988. p. 5–34.
- [29] Liaw PK, Leax TR, Williams RS, Peck MG. Acta Metall 1982;30:2071–8.

- [30] Brahma KK, Dash PK, Dattaguru B. *Int J Fatigue* 1989;11:37–41.
- [31] Yisheng W, Schijve J. *Fatigue Fract Eng Mater Struct* 1995;18:917–21.
- [32] Andersson M, Persson C, Melin S. *Int J Fatigue* 2006;28:1059–68.
- [33] Withers PJ, Bennett J, Hung YC, Preuss M. *Mater Sci Technol* 2006;22:1052–8.
- [34] Steuwer A, Edwards L, Pratihari S, Ganguly S, Peel M, Fitzpatrick ME, et al. *Nucl Instrum Methods Phys Res B* 2006;246:217–25.
- [35] Barabash R, Gao YF, Sun YN, Lee SY, Choo H, Liaw PK, et al. *Philos Mag Lett* 2008;88:553–65.
- [36] Steuwer A, Rahman M, Shterenlikht A, Fitzpatrick ME, Edwards L, Withers PJ. *Acta Mater* 2010;58:4039–52.
- [37] Lee SY, Choo H, Liaw PK, An K, Hubbard CR. *Acta Mater* 2010;59:495–502.
- [38] ASTM Standard E647-99: Standard test method for measurement of fatigue crack-growth rates, vol. 03.01. *Annual Book of ASTM Standards*; 2000. p. 591–630.
- [39] Johnson HH. *Mater Res Stand* 1965;5:442–5.
- [40] Schwalbe KH, Hellman D. *J Test Eval* 1981;9:218–20.
- [41] Irwin GR. *ASME J Appl Mech* 1957;24:361–4.
- [42] Clarke CK, Cassatt GC. *Eng Fract Mech* 1977;9:675–88.
- [43] Allen AJ, Hutchings MT, Windsor CG, Andreani C. *Adv Phys* 1985;34:445–73.
- [44] Lee SY, Rogge RB, Choo H, Liaw PK. *Fatigue Fract Eng Mater Struct*, in press. doi:10.1111/j.1460-2695.2010.01490.x.
- [45] Rice JR. *ASTM STP* 415; 1967. p. 247.